Intermetallics 105 (2019) 146–152

Contents lists available at ScienceDirect

Intermetallics

journal homepage: www.elsevier.com/locate/intermet

Nano-precipitates in severely deformed and low-temperature aged CoCrFeMnNi high-entropy alloy studied by synchrotron small-angle X-ray scattering

Yung-Chien Huang[a], Cheng-Si Tsao[a,b], Shyi-Kaan Wu[a,c,*], Chieh Lin[a], Chih-Hsuan Chen[c]

[a] Dept. of Materials Science and Engineering, National Taiwan University, Taipei, 106, Taiwan
[b] Nuclear Fuel and Materials Division, Institute of Nuclear Energy Research, Taoyuan, 325, Taiwan
[c] Dept. of Mechanical Engineering, National Taiwan University, Taipei, 106, Taiwan

ARTICLE INFO

Keywords:
High-entropy alloys
Age-hardening
Mechanical properties
Thermomechanical processing
Scattering
X-ray

ABSTRACT

The synchrotron small-angle X-ray scattering (SAXS) technique was used to reveal the evolution and growth kinetics of nano-precipitates (ppts) of severely cold-rolled CoCrFeMnNi high-entropy alloy aged at 350–500 °C for different times. The nano-ppts in the as cold-rolled alloy have a radius of ~1.2 nm, grow drastically in the early 30 min of aging at 500 °C, and reach the saturation stage at 60 min aging. The rapid increase in the size/volume fraction of the nano-ppts with the aging time is also quantitatively correlated with significant precipitation hardening, as indicated by measurements of the corresponding hardness and tensile stress-strain curve. TEM observation of the specimen aged at 500 °C for 60 min reveals many homogeneously distributed nano-ppts in the matrix, which have a radius of 2.0–2.5 nm.

1. Introduction

High entropy alloys (HEAs) have attracted great interest in recent years due to their novel mechanical and physical properties [1–8]. The most intriguing point of HEAs is that the high configurational entropy caused by the multiple components confers high phase stability [1]. One widely-investigated HEA is equiatomic CoCrFeMnNi single-phase solid solution with the FCC structure, which was reported by Cantor et al. [2] and exhibits excellent mechanical properties. Under various preparation processes and deformation conditions, the single-phase solid solution of CoCrFeMnNi alloy remains stable [9–18]. However, recent studies [19–21] have pointed out that precipitation (also regarded as decomposition) occurs in equiatomic CoCrFeMnNi alloy at medium temperatures of 600–800 °C. The second-phase precipitates (ppts) could lead to increases in strength but losses in ductility [22]. He et al. [19] found that Cr− and Mn-rich ppts form along the grain boundaries (GBs) of CoCrFeMnNi alloy creep-tested at 800 °C with a strain rate of 2.6×10^{-6} s^{-1}. Schuh et al. [22] observed that Cr-rich, FeCo-rich and NiMn-rich ppts appear in severely plastically deformed CoCrFeMnNi HEA aged at 450 °C for different times. It was proposed that the great amounts of GBs from recrystallized fine grains could act as diffusion pathways for fast transportation and nucleation sites for ppts. It has also been reported [20] that Cr-rich precipitates can be found at GBs in the non-deformed and coarse-grained alloy after prolonged aging at 700 °C. Otto et al. [23] identified several GB ppts of different phases aged at 500 °C for a long time. Zhou et al. [21] further showed that the dislocation network can stimulate the precipitation in a recovery state of annealed CoCrFeMnNi HEA after cold-rolling. The precipitation or thermal aging control of deformed HEA can be rationally manipulated to adjust the mechanical properties for various applications. However, the precipitation mechanism of deformed CoCrFeMnNi HEA is still under-investigated. According to the existing literature, the main second-phase ppts, which have been investigated by various microscopy techniques, are tens of nanometers in size. To date, no studies have focused on nano-ppts (size ≤ 5 nm). The formation of such nano-ppts and the correlation of their evolution to the mechanical properties have not been reported.

In this study, small-angle X-ray scattering (SAXS) using high-energy synchrotron radiation was employed to quantitatively reveal the morphological evolution and temperature-dependent kinetic behaviors of the nano-ppts in severely deformed CoCrFeMnNi HEA aged at 350–500 °C. The SAXS technique is a powerful tool for determining the size and volume fraction of a large number of nanoscale ppts in a bulk alloy sample. In addition to the well-investigated large ppts, SAXS can reveal the precipitation and growth kinetics of nano-ppts, which are also correlated with the alloy's mechanical properties during early

* Corresponding author. Dept. of Materials Science and Engineering, National Taiwan University, Taipei, 106, Taiwan.
E-mail address: skw@ntu.edu.tw (S.-K. Wu).

https://doi.org/10.1016/j.intermet.2018.12.003
Received 15 August 2018; Received in revised form 22 October 2018; Accepted 2 December 2018
Available online 06 December 2018
0966-9795/ © 2018 Elsevier Ltd. All rights reserved.

Table 1
The composition of homogenized CoCrFeMnNi HEA, measured by EPMA.

Element	Co	Cr	Fe	Mn	Ni
Composition (at.%)	20.22 ± 0.16	20.46 ± 0.06	19.98 ± 0.16	19.79 ± 0.10	19.54 ± 0.05

aging.

2. Experimental procedures

An equiatomic CoCrFeMnNi ingot was prepared by vacuum arc melting with six cycles of remelting to improve the homogeneity of the composition. The purity of each raw material and NiMn master alloy was better than 99.9 wt%. The ingot was then homogenized at 1200 °C for 24 h, followed by water quenching. Its composition, measured by electron probe X-ray microanalyzer (EPMA, JEOL JXA-8200), is shown in Table 1. The homogenized ingot was subsequently cold-rolled at room temperature (RT) to a thickness reduction of 85%. The specimens for SAXS measurement were cut into squares of 10 × 10 mm^2 and ground to an optimal thickness of ~20 μm at the detected area. Then the SAXS specimens were sealed into evacuated quartz tubes and aged at 350, 400 and 500 °C for different times, followed by water quenching and surface polishing. The SAXS measurements were conducted at the BL23A beamline, National Synchrotron Radiation Research Center (NSRRC), Taiwan, with high-flux collimated X-rays of 15 keV and a beam size of ~500 μm. According to standard procedures of data reduction, calibration, and background correction, each 2D SAXS pattern was azimuthally averaged into a 1D SAXS profile as a function of the scattering vector $Q = 4\pi\sin(\theta/2)/\lambda$, in which θ is the scattering angle and λ is the X-ray wavelength. The microstructural observations were also examined using a scanning transmission electron microscope (STEM, Philips Tecnai™ G^2 F20) equipped with a high angle annular dark field (HAADF) detector and energy dispersive spectroscopy (EDS). The specimens were ground to ~70 μm and punched into disks with a diameter of 3 mm. They were then twin-jet polished at about −40 °C in electrolyte of 20% nitric acid and 80% methanol (in vol.). The Vickers microhardness was measured with a hardness tester (Mitutoyo HM, Japan) with an applied load of 300 g and a loading time of 15 s. The hardness value was determined by averaging at least eight data for each specimen aged for different times. The tensile tests were conducted with a tensile testing machine (AG-IS, Shimadzu, Japan) with a maximum loading of 50 kN. The dog-boned specimens are prepared according to ASTM Standard E8 [24] and have a gauge length of 25 mm with a width of 6 mm and a thickness of 1.4 mm. The tests were performed at RT with a strain rate of 1×10^{-4} s^{-1}.

3. Results and discussion

3.1. The evolution of the SAXS profiles at different aging temperatures

Fig. 1 shows the evolution of the SAXS profiles of severely cold-rolled specimens aged at 500 °C with different aging times (t). In the SAXS profile of the as cold-rolled specimen (t = 0 min), a structure factor peak, as indicated by an arrow, can be seen at 0.16 $Å^{-1}$, signifying ppts of several nanometers in size (≤5 nm). The nano-ppt formation in the as cold-rolled CoCrFeMnNi HEA may have been due to the enhancement of the dislocation-network [21]. The advantage of the SAXS technique is that it is directly sensitive to the electron density difference between nano-ppts and the matrix, and it provides morphological analysis of the nano-ppts in a statistical way. Song et al. reported the detection of nano-ppts in deformed CoCrFeNi quaternary HEA by small-angle neutron scattering, but no further details about these nano-ppts were reported [25]. The peak position of the structure factor can be approximately related to the reciprocal of the average distance between ppts [26,27]. When the distance between ppts

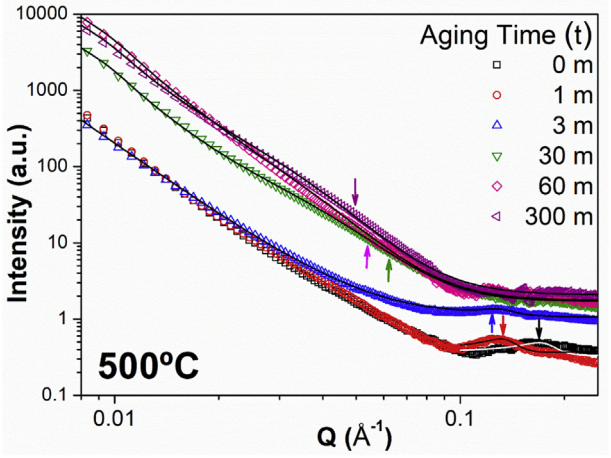

Fig. 1. Evolution of SAXS profiles of CoCrFeMnNi HEA aged at 500 °C for different times. (The solid curves represent the intensities calculated by SAXS models.)

becomes small or large, the peak position of the structure factor could move toward the high or the low Q value, respectively. The intensity of the structure factor increases with increasing the volume fraction of ppts η. For the growth step during precipitation, the volume fraction of the ppts increases and the size of the ppts grows. The volume fraction is the product of the particle number density and the particle volume. Therefore, the average distance between ppts gets large, causing the shift of peak position of the structure factor toward the low Q value. On the other hand, the shoulder position Q (or main intensity profile) of the form factor (expressed by Eq. (1) in Sec. 3.2) can be estimated by a rough rule $Q = 2\pi/D$ (D is the average ppt size). The SAXS intensity profile is the product of the form factor profile and the structure factor profile. The growth of precipitates can be evidenced by the shift of intensity peak (or structure factor peak) toward the low Q value [26–29]. As shown in Fig. 1, the nano-ppts grow as the aging time increases, as evidenced by the shift of the peak (from 0.16 $Å^{-1}$ for t = 0 min to 0.12 $Å^{-1}$ for t = 1 min), and the profile shoulder (from 0.11 $Å^{-1}$ for t = 3 min to 0.05 $Å^{-1}$ for t = 300 min, as indicated by arrows) towards the low Q value. The growth of the nano-ppts approaches stability when aging time is ≥ 60 min, indicated by the shoulder of the SAXS profiles at around 0.05 $Å^{-1}$. In addition, the upturn in intensities in the low Q region (0.008 $Å^{-1}$–0.04 $Å^{-1}$) of the specimens aged for different times is caused by the much larger particles, which shows the power-law scattering behavior, $I(Q) \propto Q^{-4}$. Such large particles have also been found in other studies [9,14,20,23]. From Fig. 1, it is clear that the volume fraction of large particles increases when the aging time is more than 30 min, as shown by the significant increase in the upturn intensity in the low Q region.

The SAXS profiles of the specimens aged at 400 °C and 350 °C for different aging times are plotted in Fig. 2(a) and (b), respectively. In Fig. 2(a), the SAXS profiles of the specimens aged at 400 °C and of those aged at 500 °C show a similar trend. Compared to the SAXS profiles of 500 °C, the peak position of the structure factor in the SAXS profiles of 400 °C, as indicated by the arrow in Fig. 2(a), shifts more slowly toward the low Q value with increasing aging time, indicating that the growth rate of the nano-ppts during 400 °C aging is lower than that during 500 °C aging. At the even lower aging temperature of 350 °C, the SAXS profiles with different aging times shown in Fig. 2(b) are almost the

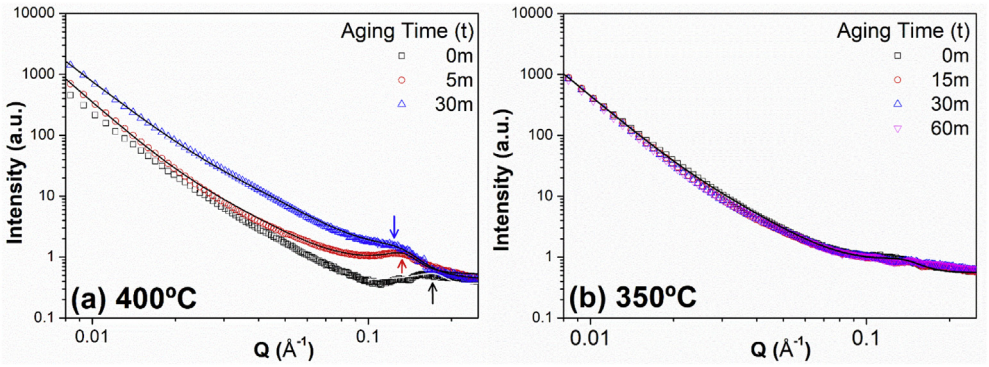

Fig. 2. Evolution of SAXS profiles of CoCrFeMnNi HEA aged at (a) 400 °C and (b) 350 °C for different times. (The solid curves represent the intensities calculated by SAXS models.)

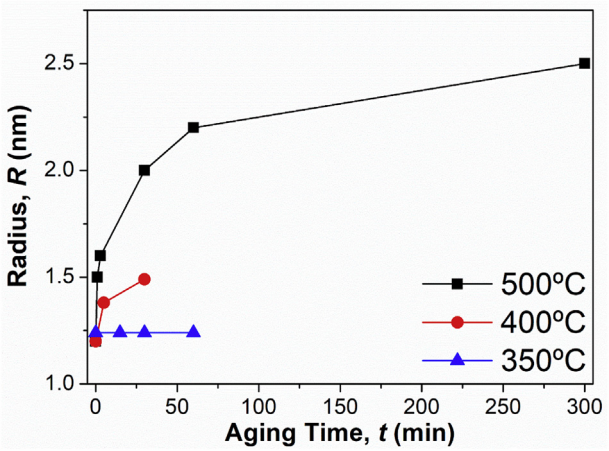

Fig. 3. Temporal behaviors of the nano-ppts' radii, R, determined by model fitting for specimens aged at 500 °C, 400 °C and 350 °C for different times.

same, suggesting little growth of the nano-ppts during 350 °C aging in the first 60 min. Apparently, according to the evolution regime and the characteristics of the SAXS profiles shown in Figs. 1 and 2, the ppts can be divided into two groups: nano-ppts and large ppts. Because the low Q range measured here is insufficient to accurately estimate the size of the large ppts, which have been reported to be tens of nanometers in size [20–23], only the nano-ppts are further studied in terms of their radius and volume fraction by quantitative SAXS analysis.

3.2. Quantitative characterization of the nano-precipitates by SAXS modeling analysis

The structure factor peak of SAXS intensity caused by the nano-ppts in specimens aged at 500 °C for 0 and 1 min can be modeled by Eq. (1) [30–34].

$$I_{nano}(Q) = \frac{\eta}{V_p}\cdot\Delta\rho^2\cdot\int_0^\infty f(r)\left[\frac{\sin(Qr) - Qr\cos(Qr)}{(Qr)^3}\right]^2 dr\cdot S(\eta, \bar{r}, Q) + b \tag{1}$$

where $\Delta\rho$ is the scattering length density contrast between ppts and the matrix, η is the volume fraction of ppts, and V_p is the average volume of ppts. The integral over particle radius r represents the form factor averaged by size distribution. The product of η and $\Delta\rho^2$ is a pre-factor constant. The relative pre-factor value can be regarded as the relative volume fraction by assuming that the $\Delta\rho^2$ value is fixed. The constant b is the incoherent scattering background. The ppts are assumed to be spherical and have the Schulz size distribution $f(r)$ with an average radius $\bar{r}$, which can be expressed by Eq. (2).

$$f(r) = \left[\frac{z+1}{\bar{r}}\right]^{z+1} r^z exp\left[-\left(\frac{z+1}{\bar{r}}r\right)\right]\frac{1}{\Gamma(z+1)} \tag{2}$$

Here, z is a parameter related to the width of the distribution from $z = (\bar{r}/\sigma_r)^2 - 1$, in which σ_r is the root-mean-square deviation from the mean size. The structure factor $S(\eta, \bar{r}, Q)$ describes the effect of hard-sphere interaction between ppts. It contains all of the information about the spatial arrangement and can be calculated as Eq. (3) [33].

$$S(\eta, \bar{r}, Q) = 1 + 4\pi\eta\int_0^\infty [h(r) - 1]\frac{sinQr}{Qr}r^2 dr \tag{3}$$

where the pair correlation function, $h(r)$, can be calculated using liquid

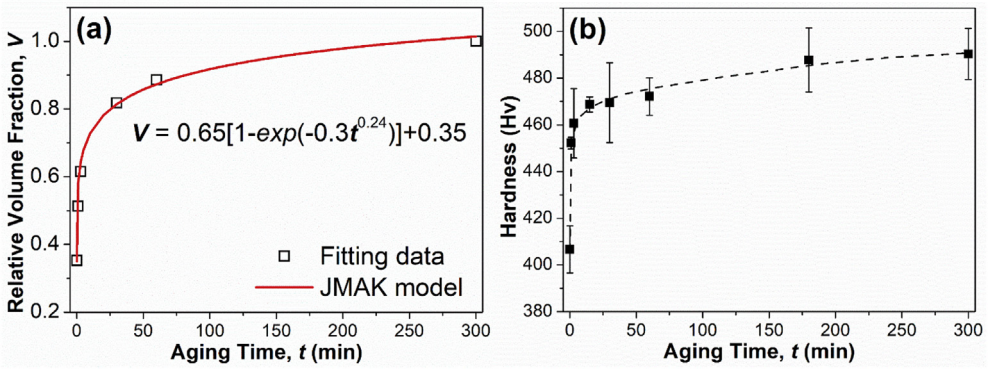

Fig. 4. (a) Evolution of the relative volume fraction, V, of the nano-ppts in CoCrFeMnNi HEA vs. aging time at 500 °C. The curve calculated from the JMAK model is also plotted. (b) Evolution of the measured hardness of specimens aged at 500 °C.

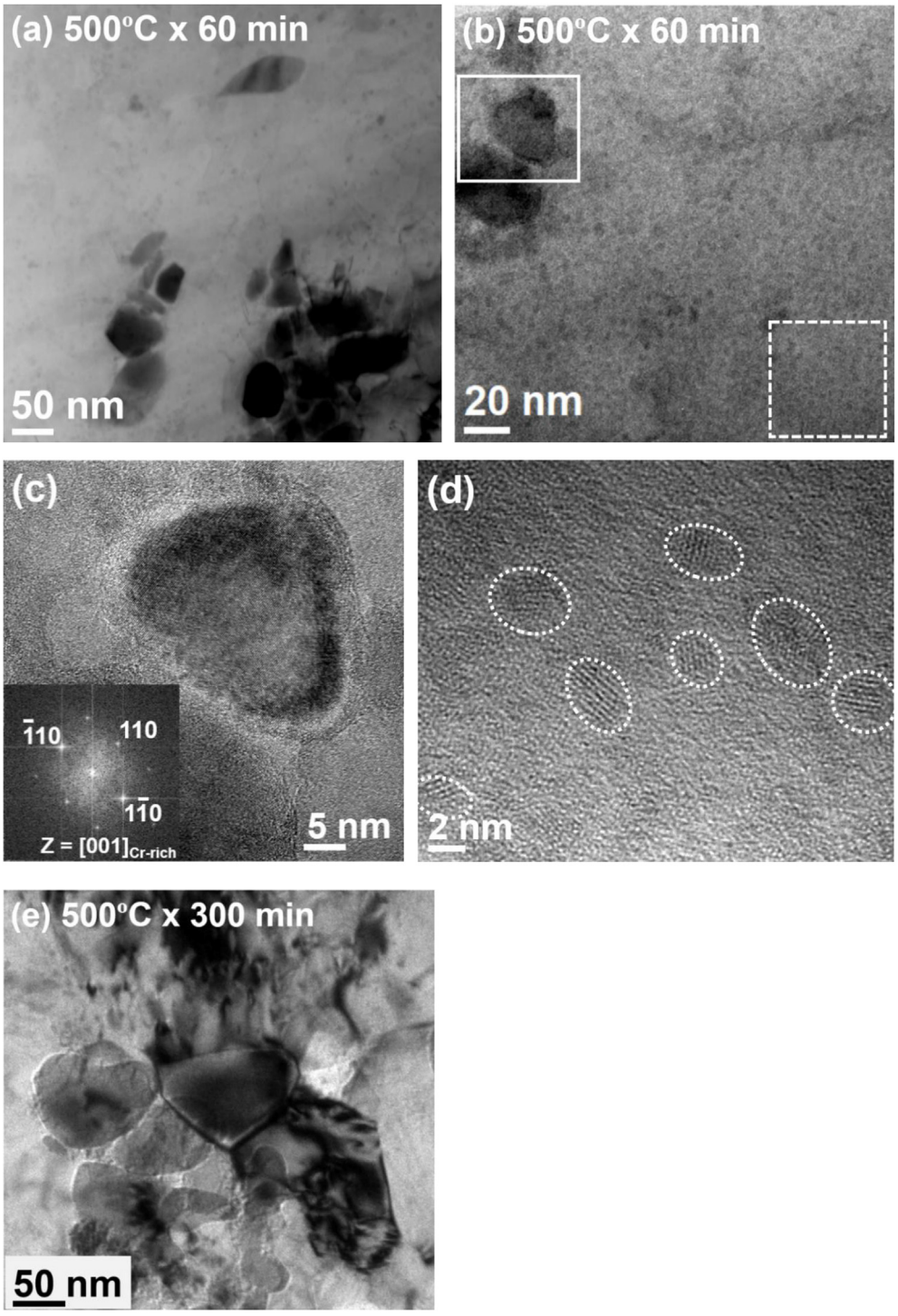

Fig. 5. The cold-rolled CoCrFeMnNi specimens aged at 500 °C for 60 min. (a) STEM image of the large ppts aggregating in the right bottom corner. (b) HRTEM bright-field image of the matrix with large ppts in the upper left corner and the nano-ppts disperse homogeneously in the matrix. (c) and (d) are the magnified images corresponding to the areas of the solid square and the dashed square in Fig. 5(b), respectively. The inset in (c) is the corresponding FFT pattern of the large ppts. The dotted circles in (d) represent the nano-ppts. (e) TEM bright-field image of the 300 min-aged specimen which indicates the significant growth of the large ppts during aging.

Table 2
The compositions of large ppts and the matrix, analyzed by HRTEM-EDS.

Element (at.%)	Co	Cr	Fe	Mn	Ni
Large ppts	9.65 ± 1.6	59.3 ± 6.7	12.8 ± 0.9	9.65 ± 1.9	8.6 ± 2.4
Matrix	19.7 ± 0.8	22.6 ± 0.5	20.8 ± 1.4	18.0 ± 0.8	18.0 ± 1.9

state theory. The peaks in the high Q region (0.1 $Å^{-1}$–0.25 $Å^{-1}$) of SAXS profiles for the specimens aged at 500 °C for 0 and 1 min can be fitted well using Eq. (1), as shown in Fig. 1 by white and black solid curves, respectively.

In the specimens aged at 500 °C for ≥3 min, the growth of the nano-ppts causes the peaks of the structure factor to be merged into the upturn intensities, so the intensity contributed by the large ppts is combined with that contributed by the nano-ppts. The sum of intensities contributed by both groups of ppts, expressed as Eq. (4), is used to fit all the SAXS profiles for resolving the morphological evolution of the nano-ppts.

$$I(Q) = I_{large}(Q) + I_{nano}(Q) \quad (4)$$

Here, the SAXS intensity resulting from the large ppts can be modeled by Eq. (5) [30–32].

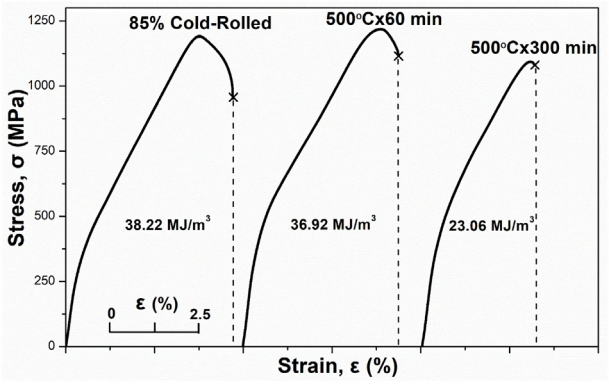

Fig. 6. The stress-strain (σ-ε) curves of cold-rolled CoCrFeMnNi specimens aged at 500 °C for 0, 60 and 300 min with a strain rate of 1×10^{-4} s^{-1}. The area under the σ-ε tensile curve is also calculated and labeled.

Table 3
The corresponding results of tensile tests for 85% cold-rolled CoCrFeMnNi specimens aged at 500 °C for 0, 60 and 300 min.

State	85% Cold-Rolled	500 °C 60 min	500 °C 300 min
Yield Stress, 0.2% offset (MPa)	372.4	468.3	489.9
Ultimate Tensile Stress (MPa)	1192	1219	1094
Elongation (%)	4.70	4.38	3.16

$$I_{large}(Q) = A \cdot \int_0^\infty g(R)\left[\frac{\sin(QR) - QR\cos(QR)}{(QR)^3}\right]^2 dR \quad (5)$$

where the constant A is a pre-factor. The large ppts have the Schulz distribution $g(R)$ in particle radius R. All the SAXS profiles for the specimens aged at 500 °C for ≥3 min fit well using Eq. (4). The characteristic peaks (0.12 $Å^{-1}$–0.16 $Å^{-1}$) and shoulders (0.03 $Å^{-1}$–0.1 $Å^{-1}$) of the SAXS profiles, marked by arrows in Fig. 1, are contributed by the nano-ppts. By the same modeling analysis, the SAXS profiles of the specimens aged at 400 °C and 350 °C for different aging times also fit well, as shown in Fig. 2(a) and (b), respectively. The temporal evolutions of the radii of the nano-ppts determined by model fitting for specimens aged at 500 °C, 400 °C and 350 °C are shown in Fig. 3. As shown in Fig. 3, the radii of the nano-ppts of 500 °C and 400 °C aged specimens grow quickly in the early aging time, with the former growing more rapidly than the latter. However, the radius of the nano-ppts in 350 °C aged specimens barely grows at all. Based on a previous study [21], the dislocation-network is supposed to enhance the nucleation of ppts. Despite the high density of dislocations can prohibit the precipitation growth, the initially rapid growth of the nano-ppts aged at 500 °C and 400 °C may be driven from the storage strain energy caused by the deformed alloy. In addition, the radius growth during 500 °C aging slows significantly after 60 min of aging, approaching a radius of 2.5 nm after 300 min of aging. This remarkable reduction of the growth rate with aging time is related to the exhaustion of the dislocations from the aging recovery effect. From Fig. 3, one can find that the growth kinetics of the nano-ppts is substantially temperature-dependent; the growth rate decreases with decreases in aging temperature, with no growth occurring at aging temperatures of ≤350 °C.

3.3. Structural evolution and kinetics of nano-precipitation correlated to hardness variation

The kinetic behavior of the nano-precipitation exhibited in 500 °C aged specimens contains the growth and saturation stages and is chosen for further analysis. The evolution of the relative volume fraction, V, of the nano-ppts determined by the SAXS modeling analysis for 500 °C aged specimens is normalized and shown in Fig. 4(a). In Fig. 4(a), the increasing trend in V seems to approach the saturation for the prolonged aging time t; i.e., the Ostward ripening or typical coarsening step, which can be predicted by the Johnson-Mehl-Avrami-Kolmogoroff (JMAK) theory [35–37]. Fig. 4(a) also presents the curve calculated from the JMAK model with $V = 0.65[1\text{-}\exp(-0.3t^{0.24})] + 0.35$. From Fig. 4(a), one can find that the curve predicted by the JMAK model fits very well to the SAXS data. The increasing V of the nano-ppts during 500 °C early aging is also found to enhance the alloy's hardness simultaneously, as indicated in Fig. 4(b). As shown in Fig. 4(b), the hardness drastically increases within 30 min of 500 °C aging. The temporal evolution of the measured hardness can be described by that of the volume fraction or the radius of nano-ppts.

The evolutions of the radius R and that of the volume fraction V of the nano-ppts are correlated to the variation of hardness. In Figs. 3 and 4, the curves of hardness Hv, radius R and volume fraction V vs. aging time t of the nano-ppts have almost the same trend, in which the values of Hv, R and V increase remarkably in the first 60 min and then saturate until 300 min of aging. Although it is hard to point out the contribution of the large ppts to the hardening effect during the early aging with the current information, the results shown in Figs. 3 and 4 provide evidence that the nano-ppts play the major role in the precipitation hardening.

3.4. TEM observation of the nano-precipitates

The cold-rolled CoCrFeMnNi specimen aged at 500 °C for 60 min was observed by STEM with EDS composition analysis to complement the SAXS results. Fig. 5(a) demonstrates a STEM image of the large ppts, revealing their density distribution in the alloy. As can be seen in Fig. 5(a), some large ppts would aggregate into a cluster while others would precipitate as individual ones. The average size of the observed large ppts is ~50 nm. Fig. 5(b) shows a typical HRTEM bright-field image of the matrix, with some large ppts visible in the upper left corner. On the other hand, the nano-ppts can also be seen in the matrix with homogeneous distribution. Fig. 5(c) and (d) are the magnified images corresponding to the areas of the solid square and the dashed square in Fig. 5(b), respectively. The corresponding fast Fourier transformation (FFT) pattern in the inset of Fig. 5(c) indicates that these large ppts have a BCC structure with a lattice constant of 2.9 Å. In Fig. 5(d), many homogeneously distributed nano-ppts, marked by dotted circles, are visible in the matrix; their radius, 2.0–2.5 nm, is consistent with the result of SAXS analysis. However, the structure of the nano-ppts can not be resolved by the corresponding FFT pattern due to noise caused by the small size of the nano-ppts and instrument limitations. Meanwhile, since the nano-ppt is too small for the TEM-EDS measurement which collects signals from a larger area than the nano-size ppt, the EDS analysis of nano-ppts would deviate from the true value considerably and thereby is not provided in the present study. Table 2 presents the EDS analysis results of the large ppts and the matrix. From Fig. 5(c) and Table 2, it can be seen that the large ppts are a Cr-rich BCC structure phase, which agrees with the results of other studies [20–23].

3.5. Relationship between the tensile property and the nano-precipitate evolution

Fig. 6 shows the stress-strain (σ-ε) curves of cold-rolled CoCrFeMnNi HEAs aged at 500 °C for different aging times. From Fig. 6, the data of the specimen's 0.2% offset yield strength (YS), ultimate tensile strength (UTS) and elongation are listed in Table 3. As shown in Table 3, the as cold-rolled specimen has high strength with moderate ductility. In the specimen aged for 60 min, which just reaches the saturation growth of the nano-ppts, both the YS and the UTS increase, but the elongation decreases. The deterioration of the elongation even leads to a decrease in the UTS in the specimen aged for 300 min, despite the slightly higher YS than that in the 60 min-aged specimen. Increasing the aging time

increases the YS with a loss in elongation.

According to Fig. 6 and Table 3, the YS increases significantly when the specimen is aged for 60 min, but this increase slows in the specimen further aged to 300 min. This trend is similar to the hardness curve shown in Fig. 4(b). However, Table 3 indicates that the aging treatment reduces the ductility. The area under the tensile σ-ε curve represents the fracture energy (U) of the specimen tested at the tensile strain rate, which is also a kind of specimen toughness and can be determined by integrating the σ-ε curve: $U = \int \sigma(\varepsilon) d\varepsilon$ [38]. In Fig. 6, the calculated U value for each σ-ε curve is labeled. The U value shows little difference between the 85% cold-rolled specimen (38.22 MJ/m^3) and the 500 °C x 60 min one (36.92 MJ/m^3), but the U value of the 500 °C x 300 min one (23.06 MJ/m^3) is significantly lower than that of the 500 °C x 60 min specimen. This result may result from the growth of the large ppts. To reveal the growth of the large ppts, Fig. 5(e) shows the TEM bright-field image of the large ppts in the 300 min-aged specimen with the size of more than 100 nm. It has been reported that the Cr-rich large ppts is a brittle phase [22,23]. Based on Fig. 5(a) and (e), during the aging treatment at 500 °C, the large ppts grow from ~50 nm for 60 min aging to more than 100 nm for 300 min aging, which is more than twice increment in the size of large ppts. Moreover, according to Fig. 5(a) and (e), the aggregation of the large ppts is supposed to further embrittle the alloy. However, during the early aging within 60 min, the homogeneous distribution of the nano-ppts acts as a strengthening phase to increase the hardness and YS with a little loss of the ductility and U value. Therefore, the appearance of the homogeneously distributed nano-ppts can enhance the mechanical properties for possible applications. This possibility of enhancement should lead to a new investigation on the optimal control of the nano-ppts by thermo-mechanical treatment.

4. Conclusions

The nano-ppts in severely deformed and low-temperature aged CoCrFeMnNi HEA have been studied by synchrotron SAXS technique. Experimental results reveal that nano-ppts appear in as cold-rolled specimens and have a radius of ~1.2 nm. These nano-ppts drastically grow during early aging at 400 °C/500 °C, with a higher growth rate at a higher aging temperature, but this growth does not occur when the specimen is aged at ≤ 350 °C. The high density dislocation-network induced by severe cold-rolling enhances the growth of the nano-ppts during the early aging. The SAXS analysis indicates that both the radius and the volume fraction of the nano-ppts aged at 500 °C grow rapidly when the aging time ≤60 min, reach the saturation stage after 60 min of aging, and approach a radius of ~2.5 nm at 300 min of aging. Moreover, the evolution of the nano-ppts in terms of the size and volume fraction is correlated with the alloy's hardness, providing evidence of the significant precipitation hardening induced by the growing nano-ppts during early aging at 500 °C. The TEM observation with EDS analysis of the specimen aged at 500 °C for 60 min reveals many homogeneously distributed nano-ppts in the matrix with a radius of 2.0–2.5 nm and the Cr-rich large ppts with some of them aggregating into a cluster. The homogeneously distributed nano-ppts can increase the hardness and YS of CoCrFeMnNi HEA, suggesting a possible way to enhance the mechanical properties for structural applications.

Acknowledgements

The authors gratefully acknowledge the financial support for this study provided by the Ministry of Science and Technology (MOST), Taiwan, under Grant Nos. MOST 106-2218-E002-025 and MOST 107-2218-E002-019.

Appendix A. Supplementary data

Supplementary data to this article can be found online at https://doi.org/10.1016/j.intermet.2018.12.003.

References

[1] J.W. Yeh, S.K. Chen, S.J. Lin, J.Y. Gan, T.S. Chin, T.T. Shun, C.H. Tsau, S.Y. Chang, Nanostructured high-entropy alloys with multiple principal elements: novel alloy design concepts and outcomes, Adv. Eng. Mater. 6 (2004) 299–303.
[2] B. Cantor, I.T.H. Chang, P. Knight, A.J.B. Vincent, Microstructural development in equiatomic multicomponent alloys, Mater. Sci. Eng. 375 (2004) 213–218.
[3] J.W. Yeh, Recent progress in high-entropy alloys, Ann. Chim.-Sci. Mat. 31 (2006) 633–648.
[4] J.W. Yeh, Physical metallurgy of high-entropy alloys, JOM (J. Occup. Med.) 67 (2015) 2254–2261.
[5] D.B. Miracle, J.D. Miller, O.N. Senkov, C. Woodward, M.D. Uchic, J. Tiley, Exploration and development of high entropy alloys for structural applications, Entropy 16 (2014) 494–525.
[6] M.H. Tsai, J.W. Yeh, High-entropy alloys: a critical review, Mater. Res. Lett. 2 (2014) 107–123.
[7] Y. Zhang, T.T. Zuo, Z. Tang, M.C. Gao, K.A. Dahmen, P.K. Liaw, Z.P. Lu, Microstructures and properties of high-entropy alloys, Prog. Mater. Sci. 61 (2014) 1–93.
[8] D.B. Miracle, O.N. Senkov, A critical review of high entropy alloys and related concepts, Acta Mater. 122 (2017) 448–511.
[9] A. Gali, E.P. George, Tensile properties of high- and medium-entropy alloys, Intermetallics 39 (2013) 74–78.
[10] B. Gludovatz, A. Hohenwarter, D. Catoor, E.H. Chang, E.P. George, R.O. Ritchie, A fracture-resistant high-entropy alloy for cryogenic applications, Science 345 (2014) 1153–1158.
[11] G. Laplanche, O. Horst, F. Otto, G. Eggeler, E.P. George, Microstructural evolution of a CoCrFeMnNi high-entropy alloy after swaging and annealing, J. Alloy. Comp. 647 (2015) 548–557.
[12] W.H. Liu, Y. Wu, J.Y. He, T.G. Nieh, Z.P. Lu, Grain growth and the Hall-Petch relationship in a high-entropy FeCrNiCoMn alloy, Scripta Mater. 68 (2013) 526–529.
[13] F. Otto, A. Dlouhy, C. Somsen, H. Bei, G. Eggeler, E.P. George, The influences of temperature and microstructure on the tensile properties of a CoCrFeMnNi high-entropy alloy, Acta Mater. 61 (2013) 5743–5755.
[14] F. Otto, N.L. Hanold, E.P. George, Microstructural evolution after thermo-mechanical processing in an equiatomic, single-phase CoCrFeMnNi high-entropy alloy with special focus on twin boundaries, Intermetallics 54 (2014) 39–48.
[15] G.D. Sathiaraj, P.P. Bhattacharjee, C.W. Tsai, J.W. Yeh, Effect of heavy cryo-rolling on the evolution of microstructure and texture during annealing of equiatomic CoCrFeMnNi high entropy alloy, Intermetallics 69 (2016) 1–9.
[16] N. Stepanov, M. Tikhonovsky, N. Yurchenko, D. Zyabkin, M. Klimova, S. Zherebtsov, A. Efimov, G. Salishchev, Effect of cryo-deformation on structure and properties of CoCrFeNiMn high-entropy alloy, Intermetallics 59 (2015) 8–17.
[17] N.D. Stepanov, D.G. Shaysultanov, N.Y. Yurchenko, S.V. Zherebtsov, A.N. Ladygin, G.A. Salishchev, M.A. Tikhonovsky, High temperature deformation behavior and dynamic recrystallization in CoCrFeNiMn high entropy alloy, Mater. Sci. Eng. 636 (2015) 188–195.
[18] Z. Wu, H. Bei, G.M. Pharr, E.P. George, Temperature dependence of the mechanical properties of equiatomic solid solution alloys with face-centered cubic crystal structures, Acta Mater. 81 (2014) 428–441.
[19] J.Y. He, C. Zhu, D.Q. Zhou, W.H. Liu, T.G. Nieh, Z.P. Lu, Steady state flow of the FeCoNiCrMn high entropy alloy at elevated temperatures, Intermetallics 55 (2014) 9–14.
[20] E.J. Pickering, R. Munoz-Moreno, H.J. Stone, N.G. Jones, Precipitation in the equiatomic high-entropy alloy CrMnFeCoNi, Scripta Mater. 113 (2016) 106–109.
[21] W. Zhou, L.M. Fu, P. Liu, X.D. Xu, B. Chen, G.Z. Zhu, X.D. Wang, A.D. Shan, M.W. Chen, Deformation stimulated precipitation of a single-phase CoCrFeMnNi high entropy alloy, Intermetallics 85 (2017) 90–97.
[22] B. Schuh, F. Mendez-Martin, B. Volker, E.P. George, H. Clemens, R. Pippan, A. Hohenwarter, Mechanical properties, microstructure and thermal stability of a nanocrystalline CoCrFeMnNi high-entropy alloy after severe plastic deformation, Acta Mater. 96 (2015) 258–268.
[23] F. Otto, A. Dlouhy, K.G. Pradeep, M. Kubenova, D. Raabe, G. Eggeler, E.P. George, Decomposition of the single-phase high-entropy alloy CrMnFeCoNi after prolonged anneals at intermediate temperatures, Acta Mater. 112 (2016) 40–52.
[24] ASTM Standard E8, Standard Test Methods for Tension Testing of Metallic Materials, ASTM International, West Conshohocken, PA, 2014, pp. 1–28.
[25] W.W. Song, A. Radulescu, L.L. Liu, W. Bleck, Study on a high entropy alloy by high energy synchrotron X-ray diffraction and small angle neutron scattering, Steel Res. Int. 88 (2017) 1700079.
[26] S. Abis, R. Caciuffo, F. Carsughi, R. Coppola, M. Magnani, F. Rustichelli, M. Stefanon, Late stages of delta' precipitation in an Al-Li alloy by small-angle neutron-scattering, Phys. Rev. B 42 (1990) 2275–2281.
[27] E. Caponetti, E.M. Daguanno, R. Triolo, S. Spooner, Kinetics of particle growth and particle composition of a commercial Al-Li alloy by means of small-angle scattering, Philos. Mag. B 63 (1991) 1201–1212.
[28] C.S. Tsao, T.L. Lin, M.S. Yu, Delta ' precipitation in Al-9.7at%Li alloy using small-angle X-ray scattering, J. Alloy. Comp. 289 (1999) 81–87.
[29] C.S. Tsao, E.W. Huang, M.H. Wen, T.Y. Kuo, S.L. Jeng, U.S. Jeng, Y.S. Sun, Phase transformation and precipitation of an Al-Cu alloy during non-isothermal heating studied by in situ small-angle and wide-angle scattering, J. Alloy. Comp. 579 (2013) 138–146.

[30] O. Glatter, O. Kratky, Small Angle X-ray Scattering, Academic Press, Cambridge, MA, USA, 1982, p. 222.
[31] A. Deschamps, F. De Geuser, On the validity of simple precipitate size measurements by small-angle scattering in metallic systems, J. Appl. Crystallogr. 44 (2011) 343–352.
[32] A. Deschamps, F. De Geuser, Quantitative characterization of precipitate microstructures in metallic alloys using small-angle scattering, Metall. Mater. Trans. 44A (2013) 77–86.
[33] J.S. Pedersen, Small-angle scattering from precipitates - analysis by use of a polydisperse hard-sphere model, Phys. Rev. B 47 (1993) 657–665.
[34] S.R. Kline, Reduction and analysis of SANS and USANS data using IGOR Pro, J. Appl. Crystallogr. 39 (2006) 895–900.
[35] M. Avrami, Kinetics of phase change I - General theory, J. Chem. Phys. 7 (1939) 1103–1112.
[36] W.A. Johnson, R.F. Mehl, Reaction kinetics in processes of nucleation and growth, T. Am. I. Min. Met. Eng. 135 (1939) 416–442.
[37] A. Kolmogoroff, Zur statistik der Kristallisationsvorgänge in metallen, Izv. Akad. Nauk SSSR Ser. Mat. 1 (3) (1937) 355–359.
[38] N.E. Dowling, Mechanical Behavior of Materials, Pearson Education, Harlow, Essex, United Kingdom, 2013, p. 133.